Inorganic Chemistry

Article

pubs.acs.org/IC

Eight-Coordinate, Stable Fe(II) Complex as a Dual ^{19}F and CEST Contrast Agent for Ratiometric pH Imaging

Kriti Srivastava,[†,§] Giuseppe Ferrauto,[‡,§] Victor G. Young, Jr.,[†] Silvio Aime,[‡] and Valérie C. Pierre*[,†]

[†]Department of Chemistry, University of Minnesota, Minneapolis, Minnesota 55455, United States

[‡]Molecular Imaging Center, Department of Molecular Biotechnologies & Health Sciences, University of Torino, 10126 Torino, Italy

Supporting Information

ABSTRACT: Accurate mapping of small changes in pH is essential to the diagnosis of diseases such as cancer. The difficulty in mapping pH accurately *in vivo* resides in the need for the probe to have a ratiometric response so as to be able to independently determine the concentration of the probe in the body independently from its response to pH. The complex Fe^{II}-DOTAm-F12 behaves as an MRI contrast agent with dual ^{19}F and CEST modality. The magnitude of its CEST response is dependent both on the concentration of the complex and on the pH, with a significant increase in saturation transfer between pH 6.9 and 7.4, a pH range that is relevant to cancer diagnosis. The signal-to-noise ratio of the ^{19}F signal of the probe, on the other hand, depends only on the concentration of the contrast agent and is independent of pH. As a result, the complex can ratiometrically map pH and accurately distinguish between pH 6.9 and 7.4. Moreover, the iron(II) complex is stable in air at room temperature and adopts a rare 8-coordinate geometry.

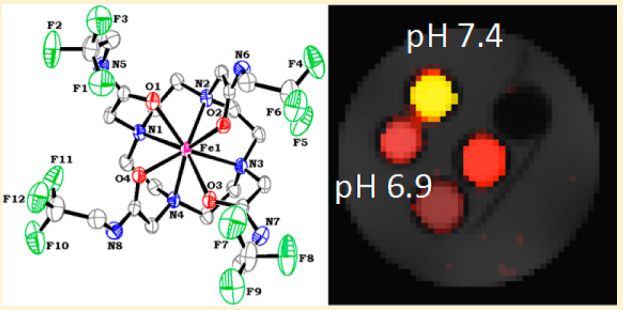

INTRODUCTION

The pH gradient between interstitial and intracellular cells is known to affect cell regulatory processes as well as drug uptake and efficiency. In cancer, for instance, poor perfusion and high metabolic rates of tumor cells lead to their hypoxic and acidic nature which, in turn, leads to higher production of lactate.[1,2] As a result, the extracellular environment of tumors is slightly more acidic than that of normal tissues.[3,4] Although small (ca. 0.7 pH units), the ability to map this variation *in vivo* is important both in terms of diagnosing, but also in predicting the response of a cancer to certain drugs.[5−7]

Magnetic resonance imaging (MRI) is a preferred *in vivo* imaging technique due to its high resolution and lack of ionizing radiation.[8] Accurate pH mapping by MRI, however, requires the use of pH-responsive contrast agents. Several such contrast agents have been reported, including Gd-based pH sensitive relaxivity agents[9−13] and chemical exchange saturation transfer (CEST) agents.[14−18] The major drawback of Gd^{III}-based probes is that signal intensity is proportional to both the concentration of the contrast agent and the pH. *In vivo* pH mapping thus assumes that the concentration of contrast agent is constant throughout the tissue, a flawed assumption given the poor perfusion of solid tumors where acidolysis occurs.[19] Consequently, pH mapping with Gd^{III}-based contrast agents can yield ambiguous results. Approaches like simultaneously injecting pH sensitive and insensitive contrast agents,[20] such as administering a cocktail of T_1 and T_2 agents,[21] ^{19}F/^{18}F MR-PET agents,[22] or ^{19}F/^{1}H probes,[23] have been used to overcome these issues. However, one cannot assume that two different probes will colocalize, hence their limited utility.

CEST probes that have two (or more) NMR-distinguishable sets of exchangeable protons with different pH responses are one solution to this problem.[24] Since these probes are ratiometric, the contrast observed is independent of the concentration of the probe. Both diamagnetic and paramagnetic CEST molecules have been reported for such applications,[15,16,18,25−27] but both have drawbacks. For instance, the mobile resonances of the diaCEST probes are too close to those of the bulk water signal and endogenous biomolecules, resulting in spillover effects and background overlap.[15] On the other hand, pH-responsive lanthanide-based paraCEST agents often require high-irradiation-power pulses in order to saturate the CEST signal. This high-irradiation power limits their translation to animal or cell studies because it leads to high deposition of energy in the tissue which causes heating.[14,25]

CEST contrast agents act by decreasing the intensity of the *bulk* water signal upon selectively saturating the resonance frequency of the mobile protons of the agent (NH, OH, or coordinated H_2O).[28] Since the exchange rate of these mobile protons is highly pH-dependent, CEST agents are uniquely suited for *in vivo* pH mapping. Given that the effectiveness of a CEST contrast agent is determined in part by a chemical shift difference ($\Delta\omega$) between water and the exchangeable ^{1}H, paramagnetic metal complexes that shift the exchangeable

Received: June 26, 2017
Published: October 5, 2017

DOI: 10.1021/acs.inorgchem.7b01629
Inorg. Chem. 2017, 56, 12206−12213

proton further away from the *bulk* water signal show improved sensitivity. Although a majority of such paramagnetic complexes have focused on lanthanide ions, recent work by J. Morrow and others have demonstrated that certain paramagnetic first row transition metals including Fe^{II} have much potential as CEST agents.[29−38] This class of compounds can also behave as pH probes. Indeed, the transition-metal-based CEST agents reported so far in the literature do show a pH-dependent response, with an increase in saturation transfer effect (ST%) at alkaline pH values.[29,30,33,35,39,40]

Notably, Fe^{II} also shows substantial advantages in the design of fluorinated MRI probes. Recent work by our group has demonstrated that fluorinated Fe^{II} complexes present much higher sensitivity than their diamagnetic analogues, and, remarkably, than their paramagnetic lanthanide ones.[41] This increase in sensitivity is due to the much shorter longitudinal relaxation times, T_1, of the fluorines and to a ratio of transverse to longitudinal relaxation times, T_2/T_1, closer to unity. Combining these two bodies of work, we postulated that a macrocyclic Fe^{II} complex bearing both exchangeable protons and fluorines, Fe^{II}-DOTAm-F12 (Figure 1), would behave as a

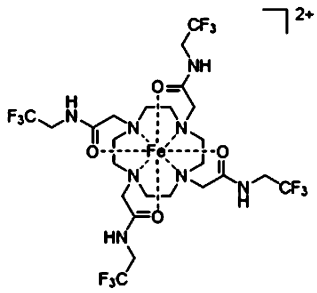

Figure 1. Chemical structure of Fe^{II}-DOTAm-F12 (**1**).

ratiometric pH-responsive MRI contrast agent whereby the CEST signal would be pH-dependent, but the ^{19}F image would not be. This, in turn, would enable accurate pH mapping without the use of multiple probes.

EXPERIMENTAL SECTION

Single Crystal X-ray Diffraction Measurements. Orange crystals suitable for X-ray diffractions were grown over several days by slow diffusion of hexane into the mixture of ethanol/toluene (2:1) solution containing the iron complex.

X-ray data were collected on a Bruker-AXS Venture PHOTON-100 diffractometer at 123(2) K.[42] The data collection was carried out using Cu Kα radiation (parabolic mirrors) with a frame time of 10 s and a detector distance of 4.0 cm. A strategy program was used to ensure complete coverage of all unique data to a resolution of 0.80 Å. All major sections of frames were collected with 0.80° steps in ω or ϕ at different detector positions in 2θ. The intensity data were corrected for absorption and decay (SADABS).[43] Final cell constants were calculated from 2798 strong reflections from the actual data collection after integration (SAINT).[43]

The structure was solved using SHELXT-2014 (Sheldrick, 2014)[44] and refined with SHELXL-2014 (Sheldrick, 2014).[45] The space group $P2_1/n$ was determined on the basis of systematic absences and intensity statistics. A direct-methods solution was calculated, which provided most non-hydrogen atoms from the E-map. Full-matrix least-squares/difference Fourier cycles were performed, which located the remaining non-hydrogen atoms. All non-hydrogen atoms were refined with anisotropic displacement parameters. The protons on the nitrogen atoms were determined from the difference map and refined with individual isotropic displacement parameters. All non-hydrogen atoms were refined with anisotropic displacement parameters. All hydrogen atoms were placed in ideal positions and refined as riding atoms with relative isotropic displacement parameters. The final full-matrix least-squares refinement converged to $R1$ = 0.0605 and $wR2$ = 0.1718 ($F2$, obsd data). See Tables S1, S4−S7 for detailed crystallographic information.

Fe^{II}-DOTAm-F12 crystallized in the space group $P2_1/n$ with pseudo-C-centering. The structure has a molecular 2-fold axis that is near the crystallographic 2-fold axis. The crystal is disordered and contains two isomers in an approximate 0.67:0.33 ratio. Several restraints (SAME, SADI, RIGU) were used to model the 12-member rings and the four methylene carbon atoms between the amide groups. There were 1268 restraints used in total. Most carbon atoms within the two rings were paired with EADP constraints if these were within about 0.4 Å. A putative partially occupied water was placed in a void region. PLATON/SQUEEZE[46] was used to check for potential disordered solvent in addition to the one partial atom found. 279 $Å^3$ of the total 4450 $Å^3$, or 6.3% of the unit cell, was determined to be void space after removing the putative, partially occupied water molecule. The total number of electrons within these voids in the unit cell was refined to 23. This suggests that some atoms are disordered beyond the point of resolution. The partially occupied water molecule was retained for the final result. The hydrogen atoms of the water were not placed but were included in the empirical formula.

The magnetic moment of Fe^{II}-DOTAm-F12 was measured both by SQUID and by NMR according to the Evans method.

Magnetic Moment: SQUID Measurement. Temperature-dependent magnetic susceptibility data were collected on a finely ground powder of Fe^{II}-DOTAM-F12 in the temperature range 2−300 K at a heating rate 1 K/min with an applied magnetic field of 1 T with a Quantum Design (MPMS-5S) SQUID magnetometer. The accurately weighed sample was loaded into a gel capsule that was then placed inside a plastic straw. The straw was mounted on a transporter rod that was placed in the magnetometer. All the data were corrected for diamagnetic contributions due to the core molecular diamagnetism of the sample using Pascal's constants.[47]

Magnetic Moment: Evans Method. The effective magnetic moment of Fe^{II}-DOTAm-F12 in solution was determined by ^1H NMR using the Evans method at 293.7 K in D_2O with 9% *t*-butanol as reference standard on a Bruker 600 spectrometer at 600 MHz using a previously published procedure.[48] Importantly, the absence of free iron in the Fe^{II}-DOTAm-F12 sample was first confirmed by a xylenol orange test. The concentration of the Fe^{II}-DOTAm-F12 in solution was measured by relaxometry after acid digestion and confirmed by ICP-MS (inductively coupled plasma mass spectrometry). For the determination of iron concentration by relaxometry, the complex was digested with nitric acid (1:10, sample/HNO_3 (v/v)) in a sealed vial at 160 °C for 24 h. Subsequently, R_1 (longitudinal relaxation rate) was measured in triplicate at 21 MHz and 25 °C using a Stelar Spinmaster relaxometer. The sample iron concentration was then assessed with a previously established calibration curve. The concentration of iron in the sample solution was also determined by ICP-MS after digestion in a microwave oven. The concentration of Fe^{II}-DOTAm-F12 was determined to be 2.27 mM.

The sample Fe^{II}-DOTAm-F12 dissolved in D_2O was placed in a capillary tube (1 mm) that was inserted in a 5 mm NMR tube containing only D_2O and *t*-butanol. The NMR spectra showed two signals for *t*-butanol; the signal from solution outside the capillary serves as a diamagnetic reference while the signal from the solution in the capillary was shifted due to the presence of paramagnetic Fe^{II}-DOTAm-F12. The observed chemical shift difference was used to calculate the mass susceptibility (χ_g) of the Fe^{II}-DOTAm-F12 in cm^3/g using eq 1

$$\chi_g = \frac{3\Delta f}{4\pi f m} + \chi_0 + \frac{[\chi_0(d_0 - d_s)]}{m} \quad (1)$$

where Δf is the chemical shift difference in Hz of the reference standard in the presence and absence of paramagnetic sample, f is the operating frequency of the spectrometer in Hz, m is mass of the substance in g/cm^3, and χ_0 is the mass susceptibility of the solvent in

DOI: 10.1021/acs.inorgchem.7b01629
Inorg. Chem. 2017, 56, 12206−12213

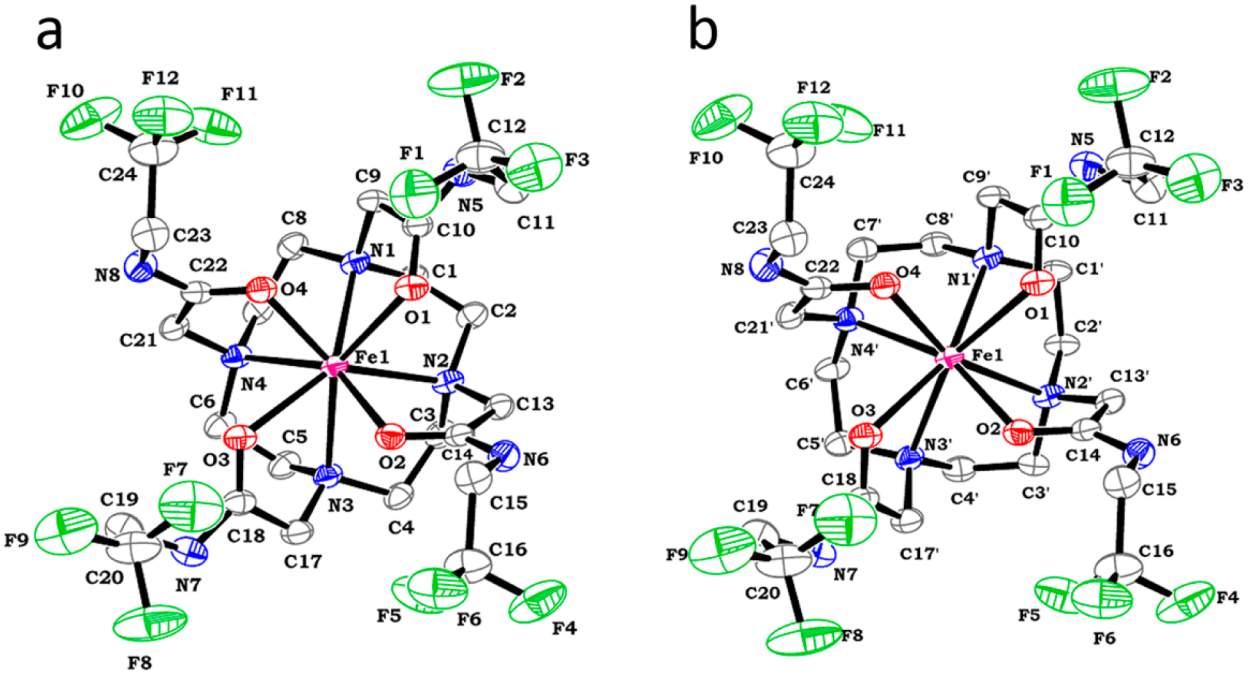

Figure 2. Molecular structure of (a) the major isomer (67%) and (b) the minor isomer (33%) of Fe^{II}-DOTAm-F12 (ORTEP, 45% probability level). Hydrogen atoms omitted for clarity.

cm^3/g. For D_2O, the reported value -0.6466×10^{-6} cm^3/g was used for χ_0. d_0 and d_s are the densities of the solvent and solution in g/cm^3, respectively. The third term was not used in the calculation because it is a negligible contribution to the overall magnetic moment.

The molar susceptibility (cm^3/mol) was calculated by multiplying the value of χ_g by the molecular weight of Fe^{II}-DOTAm-F12. The diamagnetic contributions (χ_{dia}) from the sample were estimated from Pascal's constants. These values were then used in eq 2 to calculate the paramagnetic magnetic susceptibility.

$$\chi_{measured} = \chi_{para} + \chi_{dia} \quad (2)$$

The paramagnetic susceptibly value thus obtained from eq 2 was then used to calculate the effective magnetic moment according to eq 3

$$\mu_{eff} = 2.84\sqrt{(\chi_M T)} \quad (3)$$

^{1}H and ^{19}F NMR Spectra. ^{1}H NMR spectra of Fe^{II}-DOTAm-F12 were acquired on a Varian Inova VI-500 spectrometer at 500 MHz; ^{19}F NMR spectra were acquired on a Bruker Avance, AX-400 at 377 MHz. All NMR spectra were acquired in D_2O as the solvent and at room temperature. KF ($\delta = -122.0$ ppm) was used as an external standard for ^{19}F NMR. A delay time of 30 ms and acquisition time of 64 ms were used for the collection of ^{1}H and ^{19}F NMR spectra of the Fe^{II}-DOTAm-F12 complex. Variable temperature (room temperature to 130 °C) ^{1}H NMR and ^{19}F NMR spectra were recorded in DMSO on a Bruker Avance III, AV-500, at 500 and 472 MHz, respectively.

T_2-Weighted Images. MR images were acquired at 7.1 T on a Bruker Avance 300 spectrometer equipped with a microimaging probe at 21 °C. T_2-weighted images were acquired by using a standard T_2-weighted RARE sequence with the following parameters: T_R = 5 s, T_E = 3.2 ms, isotropic 128 × 128 acquisition matrix with a FOV (field of view) of 10 mm and a slice thickness of 1 mm (matrix resolution of 0.078 mm/pixel). FOV = 10 mm × 10 mm, slice thickness = 1 mm, RF = 32.

^{19}F MR Images. ^{19}F magnetic resonance images of water solutions of Fe^{II}-DOTAm-F12 at variable pH and variable concentrations were acquired at 7.1 T on a Bruker Avance 300 spectrometer. ^{19}F images were acquired at resonant frequencies of compounds by using a FLASH sequence with the following parameters: T_E = 3.08 ms, FOV = 33 mm × 33 mm, matrix = 32 × 32, slice thickness = 5 mm, flip angle = 30°. T_R was varied from 100 to 400 ms, and NS was varied from 64 to 512. Signal-to-noise ratios were calculated by taking the ratio of the mean intensity in the circular region of interest (ROI) containing whole sample over the mean intensity in an identically sized noise region of the image. ^{19}F MRI images have been processed by applying a quadratic smoothing algorithm.

Z-Spectra and CEST MR Images. All the CEST MR images were acquired at 7.1 T on a Bruker Advance 300 spectrometer equipped with a microimaging probe at 21 °C. CEST MR images in water were acquired with phantoms consisting of one empty glass capillary as control and seven with aqueous solution of Fe^{II}-DOTAm-F12 at 10 mM concentration with pH ranging from 4 to 8. Four other aqueous solutions at pH 7.4 but with varying concentration of Fe^{II}-DOTAm-F12 were also analyzed. MR CEST phantom images of solutions in buffer (PBS 1 mM phosphates) and serum were acquired with one empty glass capillary as control along with capillaries containing 10 mM Fe^{II}-DOTAm-F12 at pH 6.9 and 7.4 in either buffer or human serum. A standard RARE (rapid acquisition with refocused echoes) spin−echo sequence (RF = 16) with an echo time of 3.2 ms and a TR value of 5 s was used (four averages). An isotropic 64 × 64 acquisition matrix with an FOV of 10 mm and a slice thickness of 1 mm were used (matrix resolution of 0.156 mm/pixel). The entire sequence was preceded by a saturation scheme consisting of a continuous rectangular wave pulse 2 s long with variable radio frequency B_1 intensity (12, 18, 24, 30, 36, or 42 μT). A frequency offset range of ±150 ppm was investigated. Image processing was carried out using custom-made software, compiled in the Matlab platform (Mathworks Inc., Natick, MA). The *Z*-spectra were interpolated by smoothing splines to identify the zero-offset on a pixel-by-pixel basis of the bulk water and to assess the correct ST% value over the entire range of frequency offsets investigated.[49] The CEST effect was calculated according to eq 4, where M_S is the intensity of the bulk water NMR signal after the irradiation on resonance ($\Delta\omega$) of the mobile proton pool and M_0 is the intensity of the bulk water NMR signal after the irradiation at $-\Delta\omega$.

$$ST\% = \left(1 - \left(\frac{M_s}{M_0}\right)\right) \times 100 \quad (4)$$

DOI: 10.1021/acs.inorgchem.7b01629
Inorg. Chem. 2017, 56, 12206−12213

Determination of Proton Exchange Rate. The exchange rate constant ($k_{ex} = 1/\tau_M$) of the NH protons was measured by the Omega plot method as reported by A. D. Sherry.[50] In the Omega plots, $[M_z/(M_0 - M_z)]$ is plotted versus $1/\omega_1^2$, where ω_1 is expressed in radians/second. The *bulk* water signal intensity measurements were carried out at the steady state after application of presaturation pulses at different B_1 values. The presaturation was carried out by using a 2 s long rectangular pulse with B_1 = 12, 18, 24, 30, and 36 μT. The τ_M value is obtained by $\tau M = \sqrt{-x_0}$, where x_0 is the x-axis intercept. Each linear plot contains 5 points, with an $R^2 \geq 0.97$ (Figure S10).

Measurements of pH by CEST and ^{19}F MR Images. The pH can be assessed from the analysis of CEST and ^{19}F MR images simply by dividing the ST% obtained in the CEST image by the signal-to-noise ratio obtained in the ^{19}F image (ST%/SNR$_{19F}$). Comparing this ratio to a calibration curve performed in the same media and magnetic field strength yields the pH.

RESULTS AND DISCUSSION

Crystal X-ray Structure of Fe^{II}-DOTAm-F12. Fe^{II}-DOTAm-F12 was synthesized as previously reported.[41] Interestingly, the single crystal X-ray structure of Fe^{II}-DOTAm-F12 (Figure 2) demonstrates that the iron(II) complex adopts a rare octacoordinated geometry. (See Tables S1, S4–S7 in SI for coordinates and select bond lengths and angles.) Although rare, 8-coordinate iron complexes are not unprecedented. Two other octacoordinated Fe(II) complexes involving tetraazamacrocycles have been reported.[35,51] At least 11 other FeN$_8$ and 13 FeO$_8$ crystal structures of 8-coordinate iron have been reported.[52,53] The geometry of the molecule can be best described as slightly distorted square-antiprismatic with an average rotation angle of −41.52° between the oxygen and nitrogen planes. The crystal structure was determined at 123(2) K and indicates disorder and the presence of two structures in an approximate 0.67:0.33 ratio (Figure 2). The structure has a 2-fold molecular axis that is near a crystallographic 2-fold axis. Note the difference observed in an Fe−N bond length of the coordinating cyclen moiety. The Fe−N distances fall mainly into two groups, a short group with the average Fe−N distance of 2.33 Å and a long group with an average Fe−N distance of 2.43 Å (Table S1). A difference of about 0.19 Å in the height of the Fe atom from the N4 plane of the cyclen moiety was also observed.

The coordinating nitrogen atoms of the cyclen moiety ∠N1−N2−N3−N4 and ∠N1′−N2′−N3′−N4′ are planar with a dihedral angle of 0.07° and 0.63°. The amide oxygen atoms also make a regular plane around the central iron atom with a dihedral angle of −0.30°. The 12-N4 ring of the cyclen moiety exists in two conformations: the average torsion angle of 57.22° gives it $\delta\delta\delta\delta$ configuration, whereas distortion provides the $\lambda\lambda\lambda\lambda$ configuration with an average torsion angle of −54.72°. For the major isomer (Figure 2a), the values of regular N−C−C−O torsion angles suggest that two of the four pendent arms have left-handed helicity (Λ) while the other two show right-handed helicity (Δ). This is uncommon for related lanthanide-based complexes that exhibit mainly one type of helicity for the pendent arms.[54,55] For the minor isomer (Figure 2b), the analysis of the N−C−C−O torsion angle due to distortion suggests a left-handed helicity (Λ) for the pendent amide arms with an average value of −23.25°. The four Fe−O bonds range from 2.18 to 2.41 Å, values that are similar to those observed for related octahedral Fe^{II} structures.[35,56,57] The 12 fluorine atoms lie between 5.22 and 6.84 Å away from the Fe^{II}, distances that are comparable to those observed for the Tm^{III} analogue of the same ligand (4.5–7.5 Å).[41] A water molecule is positioned axially on top of the Fe^{II} ion. However, unlike in the structure of the related Tm^{III} analogues,[41] the distance between the central iron atom and the oxygen of the water molecule, 3.78 Å, is too long to consider the water molecule as coordinated.

Magnetic Measurements. The variable temperature magnetic property of the bulk sample was studied by SQUID magnetometry. The measurements were carried out in both heating and cooling modes in the range 2–300 K (Figure S3). The magnetization data was simulated using the julX program for exchange coupled systems.[58] The simulation was based on the spin-Hamiltonian operator for mononuclear complexes shown in eq 5. The best fit was obtained with spin S = 2, axial zero-field splitting parameter D = 9, rhombicity E/D = 0, and g = 1.99 including 9% of paramagnetic impurity with S = 0.5. From this fitting, the effective magnetic moment (μ_{eff}) of Fe^{II}-DOTAm-F12 at 298 K was determined to be 4.60 μ_B. This value is close to that calculated for the spin only value (S = 2) for high-spin Fe^{II} (4.90 μ_B), indicating that the complex is in a high-spin state at room temperature. The value of the effective magnetic moment remains nearly constant in the range 30–300 K.

$$\vec{\mathcal{H}} = g\beta\vec{\hat{S}}\cdot\vec{B} + D\left[\hat{S}_z^2 - \frac{1}{3}S(S+1) + \frac{E}{D(\hat{S}_x^2 - \hat{S}_y^2)}\right] \quad (5)$$

The effective magnetic moment of the Fe^{II} complex was further studied by solution NMR spectrometry according to Evans' method.[48] A μ_{eff} of ∼6.0 μ_B was determined by solution NMR. Although the effective magnetic moment value determined in solution is different than that determined in the solid state, both measurements suggest a high-spin state for the Fe^{II}-DOTAm-F12 complex. The origin of the discrepancy between the magnetic moment determined in solution and the solid state is not fully understood at this point but could potentially be due to a change in the environmental condition of the complex between solution and the solid state. Such differences are not uncommon and have been observed previously for other complexes as well.[59–61]

To probe further the behavior of Fe^{II}-DOTAm-F12 in solution, variable temperature ^{1}H and ^{19}F NMR were recorded. The ^{1}H NMR spectra of the complex in DMSO shows a decrease in hyperfine shift with increasing temperature (Figure S8). In contrast, a smaller change in the chemical shifts of the ^{19}F nuclei is observed with increasing temperature (Figure S9). This process is reversible and confirmed that the Fe^{II} complex is stable up to 130 °C.

^{19}F and CEST-MRI. The ^{19}F NMR spectrum of Fe^{II}-DOTAm-F12 in water (Figure S2) indicates that all ^{19}F nuclei remain equivalent by NMR. This strongly suggests that, in solution at room temperature, the pseudo-4-fold symmetry of the iron complex is maintained and that the Fe^{II} ion remains 8-coordinate. In addition, the presence of a single peak suggests that only one isomer is present in solution, and that the four CF_3 arms rotate faster than the NMR time scale.

As predicted, ^{19}F MR images of solutions of Fe^{II}-DOTAm-F12 indicate that the signal-to-noise ratio (SNR) of the ^{19}F phantom increases linearly with the concentration of the iron complex (Figure S7a,b). The limit of detection of the iron complex by ^{19}F MRI, which is the concentration needed to achieve an SNR of 3, is 2 mM. Interestingly, the limit-of-detection of the complex is similar by ^{19}F and ST$_{weighted}$

DOI: 10.1021/acs.inorgchem.7b01629
Inorg. Chem. 2017, 56, 12206–12213

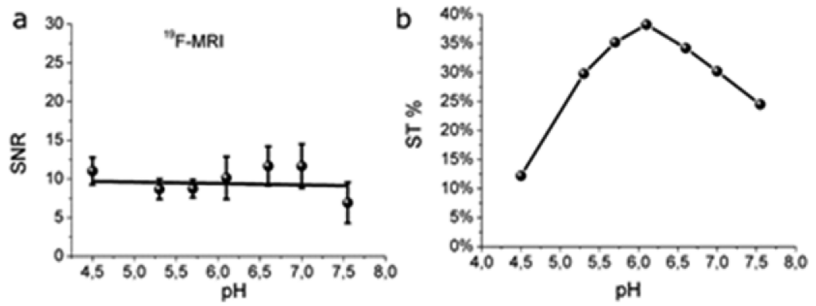

Figure 3. (a) Signal-to-noise ratio in ^{19}F MR image of a phantom made by glass capillaries containing 10 mM Fe^{II}-DOTAm-F12 complex in water as a function of pH. (b) ST% vs pH from $ST_{weighted}$ images upon irradiation at 39 ppm of phantom described in part a.

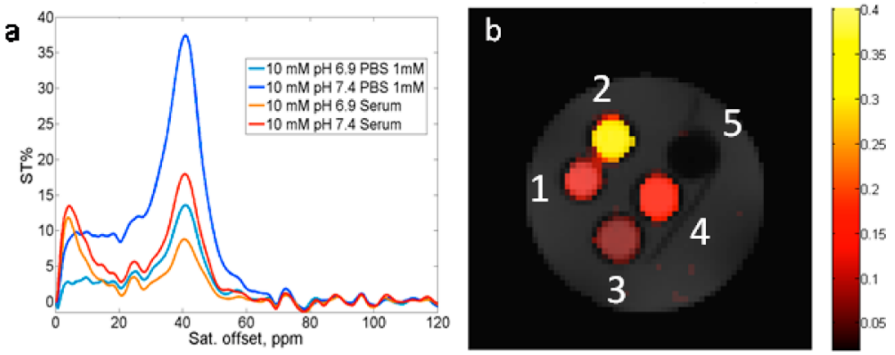

Figure 4. (a) ST-spectra and (b) $ST_{weighted}$ images upon irradiation at 39 ppm of Fe^{II}-DOTAm-F12 in (1) phosphate buffered saline (PBS) at pH 6.9, (2) PBS at pH 7.4, (3) human serum at pH = 6.9, (4) human serum at pH 7.4, and (5) empty capillary tube. Experimental conditions: [Fe^{II}-DOTAm-F12] = 10 mM, B_1 = 30 μT.

(CEST) MRI (*vide infra*), indicating that the contrast agent can be visualized by either modality with the same sensitivity, an important parameter for ratiometric MR imaging. Importantly, the intensity of the ^{19}F signal of the probe is independent of pH (Figure 3a). Capillary tubes filled with the same concentration of [Fe^{II}-DOTAm-F12] but at different pH still display the same signal intensity in a ^{19}F MR image (Figure 5, tubes 1−4). Although not surprising, this independence of the ^{19}F MR image on pH is crucial to the ability of the complex to behave as its own internal standard. As can be seen in Figure 5, because the ^{19}F signal intensity is only dependent on the concentration of Fe^{II}-DOTAm-F12 and not on the pH, the ^{19}F MR image can accurately map the concentration of the contrast agent throughout a sample or tissue.

The NH groups of the arms are also chemically equivalent and are close to the paramagnetic Fe^{II} center. As a result, the ^{1}H NMR signal of the exchangeable protons is well-shifted 39 ppm away from the *bulk* water signal. Since the amide protons exchange with bulk water protons in a pH-dependent manner, Fe^{II}-DOTAm-F12 was anticipated to behave as a pH-responsive CEST agent. The magnitude of saturation transfer indeed increases substantially from ∼8% at pH 4 to a maximum 40% at pH 6.2 (in aqueous solution). Interestingly, further increasing the pH to 8 results in a substantial decrease of the CEST effect to ∼25% ST. Notably, the decrease in ST% from pH 6.0 to 8.0 is opposite to the trend normally observed with paraCEST agents.[30,62,63] Generally, the saturation transfer increases as the pH increases to 8 due to a base catalyzed increase of the proton exchange rate.[39,40] However, the exchange rates of amide protons are well-known to depend on the electronic properties of the appended amide group as well as pH. The presence of CF_3, an electron withdrawing substituent, in close proximity of the amide enhances the acidity of its proton by pulling the electron density away from the nitrogens. This facilitates deprotonation of the amide and the development of negative charge on the nitrogen that needs to be stabilized in order to observe the CEST effect. It was previously shown that neutral electronegative substituents tend to stabilize this charge thereby shifting the maxima of saturation transfer toward lower pH value.[64] Negatively charged electron withdrawing groups, however, have the opposite effect since they destabilize the charged species.[65] Moreover, coordination of the amide oxygen to the central metal ion involves sharing the amide nitrogen's lone pair. This sharing also increases the acidity of the amide proton and ultimately affects their pH sensitivity range.

In Fe^{II}-DOTAm-F12, since these two opposite factors are both present, a maximum in the saturation transfer is observed at slightly acidic pH (Figures 3b and 5, and Figure S6). This distinguishes the fluorinated iron complex from most paraCEST agents for which the maxima of saturation transfer are observed in the basic pH range.[39,40] The decrease in the CEST intensity at a higher pH value is ascribable to the increase in the exchange rate of the amide proton (k_{ex}). Faster exchange rates increase saturation transfer, but only to a point beyond which a too fast exchange rate causes NMR peaks to coalesce which in turn decreases ST%. Notably, the presence of a maximum in the ST% response is not detrimental to biomedical applications. The pH of extracellular space where MRI contrast agents that are administered intravenously can accumulate is rarely lower than pH 6. pH mapping is particularly relevant to diagnosis and monitoring of cancer. In cancer tissues, the extracellular pH rarely decreases by more than 1 pH unit. The extracellular pH of normal tissue is usually pH 7.4; on the other extreme, under chronic acidosis it

DOI: 10.1021/acs.inorgchem.7b01629
Inorg. Chem. 2017, 56, 12206−12213

decreases to no less than 6.7.[3,4] Importantly, ST% changes linearly in pH range 6−7.5, which is the pH range of physiological concern to cancer imaging.

The amide proton residence time ($\tau_m = 1/k_{ex}$) of Fe^{II}-DOTAm-F12 has been measured in phosphate buffered saline (PBS) and human serum at 21 °C according to the Omega plot method reported by A. D. Sherry et al. (Figure S10 and Table S2).[50] In both media, τ_m decreases substantially as the pH increases from 6.9 to 7.4, although a much bigger decrease is observed in serum (58%) than in PBS (24%). This substantial change in τ_m and in the corresponding ST% strongly suggests that the Fe^{II} complex could accurately map out small differences in pH, such as those occurring in the extracellular environments of tumors. In view of these possible *in vivo* applications, *Z*-spectra, ST% spectra, and $ST_{weighted}$ images of solutions of Fe^{II}-DOTAm-F12 in PBS and human serum at both pH 7.4 and 6.9, the pH of normal and hypoxic extracellular environments, respectively, were obtained (Figure 4a,b). As expected, the increase in k_{ex} from pH 6.9 to 7.4, which also broadens the NMR peak of the amide proton at higher pH values (Figure S6), results in a significant increase in the CEST effect. Images at pH 7.4 appear noticeably brighter than those at pH 6.9 (Figure 4b). Note that the magnitude of the CEST effect is also affected by other constituents of serum, as a ca. 10% decrease in CEST intensity is observed between serum and buffer. The additional peak shifted 2−3 ppm away from water that is present in serum but not PBS which is due to the endogenous proteins of serum.[66]

As for all CEST contrast agents, the intensity of the MR signal is a function of the concentration of the agents. For Fe^{II}-DOTAm-F12, a direct relationship is observed by NMR between the concentration of the iron complex and the intensity of the CEST peak (Figure S5). Analysis of $ST_{weighted}$ phantoms, however, indicates that the increase in ST% and signal intensity reaches a plateau above 4 mM (Figure S7c,d). The limit of detection of Fe^{II}-DOTAm-F12 by CEST, defined as the concentration of the iron complex needed to achieve a ST% of 5%, is ca. 2 mM at pH 7.4. The saturation transfer of Fe^{II}-DOTAm-F12 indicates that its sensitivity is in the same order of magnitude as that of other previously reported Fe^{II}-based paraCEST agents at both pH 6.9 and 7.4 (Table S3).[29,30,33,39,40] The chemical shift of the exchangeable proton pool is far from the *bulk* water signal ($\Delta\omega$ = 39 ppm), but not completely outside the region in which the magnetization transfer effect (MTC) of water bound to solid tissue is present.[67] The MTC effect depends strongly on the B_1 field used with a broader MTC signal obtained at higher B_1. At the B_1 fields used in this work, the MTC effect extends to ca. 100 ppm from *bulk* water. Therefore, it is anticipated that Fe^{II}-DOTAm-F12 will be less sensitive in tissue than in water.[68]

Moreover, an expected rise in the saturation transfer has been observed upon increasing the irradiation power of the presaturation pulse (Figure S4). Note, however, that practically, for *in vivo* applications, high B_1 values have to be avoided since more intense presaturation pulses lead to higher specific absorption rate (SAR) of energy in the imaged tissue, which is detrimental to the patient's health.

Notably, the signal intensity observed in the ^{19}F MR image is a function only of the concentration of the probe and is independent of pH (Figure 5, left). On the other hand, the signal intensity observed in $ST_{weighted}$ CEST images is a function both of the concentration of the probe and of the pH (Figure 5, right). This different response toward pH in the two modalities

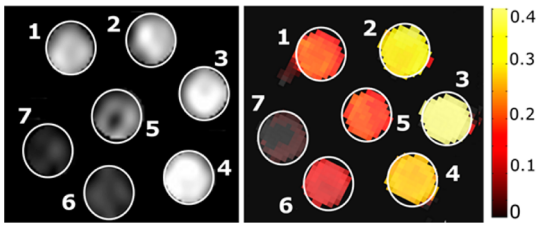

Figure 5. ^{19}F (left) and CEST $ST_{weighted}$ (right) phantom images of Fe^{II}-DOTAm-F12 in water at variable pH and/or probe concentration: (1) [Fe^{II}-DOTAm-F12] = 10 mM, pH 5.0; (2) [Fe^{II}-DOTAm-F12] = 10 mM, pH 5.5; (3) [Fe^{II}-DOTAm-F12] = 10 mM, pH 6.2; (4) [Fe^{II}-DOTAm-F12] = 10 mM, pH 7.0; (5) [Fe^{II}-DOTAm-F12] = 6 mM, pH 7.0; (6) [Fe^{II}-DOTAm-F12] = 4 mM, pH 7.0; (7) [Fe^{II}-DOTAm-F12] = 2 mM, pH 7.0. Note that the signal intensity observed in the ^{19}F phantom is dependent on the concentration of the probe (tubes 1, 5, 6, and 7) but is independent of the pH (tubes 1−4), thereby enabling determination of the spatial distribution of the probe independently of the pH. The pH can then be determined from the intensity of the CEST image.

(^{19}F and CEST MRI) advantageously enables rapid determination of the pH ratiometrically even under conditions where the concentration of the probe is unknown. The spatial distribution of the probe can be directly assessed by the ^{19}F MR image. The pH can then be assessed from the analysis of the CEST and ^{19}F MR images simply by dividing the ST% obtained in the CEST image by the signal-to-noise ratio obtained in the ^{19}F image. Comparing this ratio to a calibration curve performed in the same media, temperature, and magnetic field strength yields the pH.

CONCLUSION

Fe^{II}-DOTAm-F12 behaves as an MRI contrast with dual ^{19}F and CEST modality. The sensitivity of the complex is the same in both modalities, with a limit of detection at ca. 2 mM. The magnitude of the CEST response is dependent both on the concentration of the complex and on the pH, with a maximum of saturation transfer at pH 6.0 in water. On the other hand, the SNR of the ^{19}F signal is only dependent on the concentration of the complex and is independent of pH. This difference in response in the two modalities enables the complex to map pH changes ratiometrically. The distribution of the complex can be determined directly by the ^{19}F MR images, which in turn enables accurate determination of pH changes via $ST_{weighted}$ images. The substantial change in ST% enables accurate pH mapping within a narrow pH range representative of hypoxic tissues. Interestingly, Fe^{II}-DOTAm-F12 exists as a rare 8-coordinate complex. The high-spin Fe(II) complex is stable in air at room temperature for long periods of time (year).

ASSOCIATED CONTENT

Supporting Information

The Supporting Information is available free of charge on the ACS Publications website at DOI: 10.1021/acs.inorgchem.7b01629.

Variable temperature NMR; ^1H and ^{19}F NMR characterization of metal complexes; X-ray crystallographic data; SQUID magnetometry data; *Z* and ST% spectra as a function of B_1, concentration of complex, and pH; ^{19}F MR images; τ_M values; and comparison of parameters with other reported Fe^{II}-based CEST agents (PDF)

DOI: 10.1021/acs.inorgchem.7b01629
Inorg. Chem. 2017, 56, 12206−12213

Accession Codes

CCDC 1506168 contains the supplementary crystallographic data for this paper. These data can be obtained free of charge via www.ccdc.cam.ac.uk/data_request/cif, or by emailing data_request@ccdc.cam.ac.uk, or by contacting The Cambridge Crystallographic Data Centre, 12 Union Road, Cambridge CB2 1EZ, UK; fax: +44 1223 336033.

AUTHOR INFORMATION

Corresponding Author

*E-mail: pierre@umn.edu.

ORCID

Valérie C. Pierre: 0000-0002-0907-8395

Author Contributions

§K.S. and G.F. contributed equally. The manuscript was written through contributions of all authors. All authors have given approval to the final version of the manuscript.

Notes

The authors declare no competing financial interest.

ACKNOWLEDGMENTS

This work was supported by the National Science Foundation Grant CAREER 1151665 (V.C.P.), by the NIH Clinical and Translational Science Award at the University of Minnesota (8UL1TR000114), and by the European H2020 IDentIFY grant (S.A.). G.F. was supported by an FIRC (Fondazione Italiana per la Ricerca sul Cancro AIRC) fellowship. The authors thank Dr. Sylvie Pailloux for her help with the manuscript preparation.

REFERENCES

(1) Warburg, O. H.; Dickens, F. *The Metabolism of Tumours*; Constable: London, 1930.

(2) Warburg, O. On the origin of cancer cells. *Science* **1956**, *123*, 309−314.

(3) Wike-Hooley, J. L.; Haveman, J.; Reinhold, H. S. The relevance of tumour pH to the treatment of malignant disease. *Radiother. Oncol.* **1984**, *2*, 343−366.

(4) Vaupel, P.; Kallinowski, F.; Okunieff, P. Blood flow, oxygen and nutrient supply, and metabolic microenvironment of human tumors: a review. *Cancer Res.* **1989**, *49*, 6449−6465.

(5) Thews, O.; Gassner, B.; Kelleher, D. K.; Schwerd, G.; Gekle, M. Impact of extracellular acidity on the activity of P-glycoprotein and the cytotoxicity of chemotherapeutic drugs. *Neoplasia* **2006**, *8*, 143−152.

(6) Lotz, C.; Kelleher, D. K.; Gassner, B.; Gekle, M.; Vaupel, P.; Thews, O. Role of the tumor microenvironment in the activity and expression of the p-glycoprotein in human colon carcinoma cells. *Oncol. Rep.* **2007**, *17*, 239−244.

(7) Wojtkowiak, J. W.; Verduzco, D.; Schramm, K. J.; Gillies, R. J. Drug Resistance and Cellular Adaptation to Tumor Acidic pH Microenvironment. *Mol. Pharmaceutics* **2011**, *8*, 2032−2038.

(8) Pierre, V. C.; Allen, M. J.; Caravan, P. Contrast agents for MRI: 30+ years and where are we going? *JBIC, J. Biol. Inorg. Chem.* **2014**, *19*, 127−131.

(9) Aime, S.; Botta, M.; Crich, S. G.; Giovenzana, G.; Palmisano, G.; Sisti, M. Novel Paramagnetic Macromolecular Complexes Derived from the Linkage of a Macrocyclic Gd(III) Complex to Polyamino Acids through a Squaric Acid Moiety. *Bioconjugate Chem.* **1999**, *10*, 192−199.

(10) Zhang, S.; Wu, K.; Sherry, A. D. A novel pH-sensitive MRI contrast agent. *Angew. Chem., Int. Ed.* **1999**, *38*, 3192−3194.

(11) Woods, M.; Kiefer, G. E.; Bott, S.; Castillo-Muzquiz, A.; Eshelbrenner, C.; Michaudet, L.; McMillan, K.; Mudigunda, S. D. K.; Ogrin, D.; Tircso, G.; Zhang, S.; Zhao, P.; Sherry, A. D. Synthesis, Relaxometric and Photophysical Properties of a New pH-Responsive MRI Contrast Agent: The Effect of Other Ligating Groups on Dissociation of a p-Nitrophenolic Pendant Arm. *J. Am. Chem. Soc.* **2004**, *126*, 9248−9256.

(12) Tóth, E.; Bolskar, R. D.; Borel, A.; Gonzalez, G.; Helm, L.; Merbach, A. E.; Sitharaman, B.; Wilson, L. J. Water-Soluble Gadofullerenes: Toward High-Relaxivity, pH-Responsive MRI Contrast Agents. *J. Am. Chem. Soc.* **2005**, *127*, 799−805.

(13) Kálmán, F. K.; Woods, M.; Caravan, P.; Jurek, P.; Spiller, M.; Tircsó, G.; Kiraly, R.; Brücher, E.; Sherry, A. D. Potentiometric and Relaxometric Properties of a Gadolinium-Based MRI Contrast Agent for Sensing Tissue pH. *Inorg. Chem.* **2007**, *46*, 5260−5270.

(14) Delli Castelli, D.; Terreno, E.; Aime, S. YbIII-HPDO3A: A Dual pH- and Temperature-Responsive CEST Agent. *Angew. Chem., Int. Ed.* **2011**, *50*, 1798−1800.

(15) Longo, D. L.; Sun, P. Z.; Consolino, L.; Michelotti, F. C.; Uggeri, F.; Aime, S. A General MRI-CEST Ratiometric Approach for pH Imaging: Demonstration of in Vivo pH Mapping with Iobitridol. *J. Am. Chem. Soc.* **2014**, *136*, 14333−14336.

(16) Longo, D. L.; Dastrù, W.; Digilio, G.; Keupp, J.; Langereis, S.; Lanzardo, S.; Prestigio, S.; Steinbach, O.; Terreno, E.; Uggeri, F.; Aime, S. Iopamidol as a responsive MRI-chemical exchange saturation transfer contrast agent for pH mapping of kidneys: In vivo studies in mice at 7 T. *Magn. Reson. Med.* **2011**, *65*, 202−211.

(17) Zhang, S.; Zhou, K.; Huang, G.; Takahashi, M.; Dean Sherry, A.; Gao, J. A novel class of polymeric pH-responsive MRI CEST agents. *Chem. Commun.* **2013**, *49*, 6418−6420.

(18) Wang, X.; Wu, Y.; Soesbe, T. C.; Yu, J.; Zhao, P.; Kiefer, G. E.; Sherry, A. D. A pH-Responsive MRI Agent that Can Be Activated Beyond the Tissue Magnetization Transfer Window. *Angew. Chem., Int. Ed.* **2015**, *54*, 8662−8664.

(19) Raghunand, N.; Gatenby, R. A.; Gillies, R. J. Microenvironmental and cellular consequences of altered blood flow in tumours. *Br. J. Radiol.* **2003**, *76*, S11−S22.

(20) Raghunand, N.; Howison, C.; Sherry, A. D.; Zhang, S.; Gillies, R. J. Renal and systemic pH imaging by contrast-enhanced MRI. *Magn. Reson. Med.* **2003**, *49*, 249−257.

(21) Martinez, G. V.; Zhang, X.; Garcia-Martin, M. L.; Morse, D. L.; Woods, M.; Sherry, A. D.; Gillies, R. J. Imaging the extracellular pH of tumors by MRI after injection of a single cocktail of T1 and T2 contrast agents. *NMR Biomed.* **2011**, *24*, 1380−1391.

(22) Frullano, L.; Catana, C.; Benner, T.; Sherry, A. D.; Caravan, P. Bimodal MR-PET Agent for Quantitative pH Imaging. *Angew. Chem., Int. Ed.* **2010**, *49*, 2382−2384.

(23) Gianolio, E.; Napolitano, R.; Fedeli, F.; Arena, F.; Aime, S. Poly-β-cyclodextrin based platform for pH mapping via a ratiometric 19F/1H MRI method. *Chem. Commun.* **2009**, 6044−6046.

(24) Ward, K. M.; Balaban, R. S. Determination of pH using water protons and chemical exchange dependent saturation transfer (CEST). *Magn. Reson. Med.* **2000**, *44*, 799−802.

(25) Wu, Y.; Soesbe, T. C.; Kiefer, G. E.; Zhao, P.; Sherry, A. D. A Responsive Europium(III) Chelate That Provides a Direct Readout of pH by MRI. *J. Am. Chem. Soc.* **2010**, *132*, 14002−14003.

(26) Sheth, V. R.; Li, Y.; Chen, L. Q.; Howison, C. M.; Flask, C. A.; Pagel, M. D. Measuring in vivo tumor pHe with CEST-FISP MRI. *Magn. Reson. Med.* **2012**, *67*, 760−768.

(27) Chen, L. Q.; Howison, C. M.; Jeffery, J. J.; Robey, I. F.; Kuo, P. H.; Pagel, M. D. Evaluations of extracellular pH within in vivo tumors using acidoCEST MRI. *Magn. Reson. Med.* **2014**, *72*, 1408−1417.

(28) Terreno, E.; Castelli, D. D.; Aime, S. Encoding the frequency dependence in MRI contrast media: the emerging class of CEST agents. *Contrast Media Mol. Imaging* **2010**, *5*, 78−98.

(29) Dorazio, S. J.; Tsitovich, P. B.; Siters, K. E.; Spernyak, J. A.; Morrow, J. R. Iron(II) PARACEST MRI Contrast Agents. *J. Am. Chem. Soc.* **2011**, *133*, 14154−14156.

(30) Dorazio, S. J.; Tsitovich, P. B.; Gardina, S. A.; Morrow, J. R. The reactivity of macrocyclic Fe(II) paraCEST MRI contrast agents towards biologically relevant anions, cations, oxygen or peroxide. *J. Inorg. Biochem.* **2012**, *117*, 212−219.

DOI: 10.1021/acs.inorgchem.7b01629
Inorg. Chem. 2017, 56, 12206−12213

(31) Dorazio, S. J.; Morrow, J. R. The Development of Iron(II) Complexes as ParaCEST MRI Contrast Agents. *Eur. J. Inorg. Chem.* **2012**, *2012*, 2006−2014.
(32) Dorazio, S. J.; Olatunde, A. O.; Tsitovich, P. B.; Morrow, J. R. Comparison of divalent transition metal ion paraCEST MRI contrast agents. *JBIC, J. Biol. Inorg. Chem.* **2014**, *19*, 191−205.
(33) Tsitovich, P. B.; Morrow, J. R. Macrocyclic ligands for Fe(II) paraCEST and chemical shift MRI contrast agents. *Inorg. Chim. Acta* **2012**, *393*, 3−11.
(34) Jeon, I.-R.; Park, J. G.; Haney, C. R.; Harris, T. D. Spin crossover iron(ii) complexes as PARACEST MRI thermometers. *Chem. Sci.* **2014**, *5*, 2461−2465.
(35) Olatunde, A. O.; Bond, C. J.; Dorazio, S. J.; Cox, J. M.; Benedict, J. B.; Daddario, M. D.; Spernyak, J. A.; Morrow, J. R. Six, Seven or Eight Coordinate Fe(II), Co(II) or Ni(II) Complexes of Amide-Appended Tetraazamacrocycles for ParaCEST Thermometry. *Chem. - Eur. J.* **2015**, *21*, 18290−18300.
(36) Tsitovich, P. B.; Cox, J. M.; Spernyak, J. A.; Morrow, J. R. Gear Up for a pH Shift: A Responsive Iron(II) 2-Amino-6-picolyl-Appended Macrocyclic paraCEST Agent That Protonates at a Pendent Group. *Inorg. Chem.* **2016**, *55*, 12001−12010.
(37) Tsitovich, P. B.; Cox, J. M.; Benedict, J. B.; Morrow, J. R. Six-coordinate Iron(II) and Cobalt(II) paraSHIFT Agents for Measuring Temperature by Magnetic Resonance Spectroscopy. *Inorg. Chem.* **2016**, *55*, 700−716.
(38) Burns, P. J.; Cox, J. M.; Morrow, J. R. Imidazole-Appended Macrocyclic Complexes of Fe(II), Co(II), and Ni(II) as ParaCEST Agents. *Inorg. Chem.* **2017**, *56*, 4545−4554.
(39) Dorazio, S. J.; Morrow, J. R. Iron(II) complexes containing octadentate tetraazamacrocycles as paraCEST magnetic resonance imaging contrast agents. *Inorg. Chem.* **2012**, *51*, 7448−7450.
(40) Dorazio, S. J.; Olatunde, A. O.; Spernyak, J. A.; Morrow, J. R. CoCEST: cobalt(II) amide-appended paraCEST MRI contrast agents. *Chem. Commun.* **2013**, *49*, 10025−10027.
(41) Srivastava, K.; Weitz, E. A.; Peterson, K. L.; Marjanska, M.; Pierre, V. C. Fe- and Ln-DOTAm-F12 Are Effective Paramagnetic Fluorine Contrast Agents for MRI in Water and Blood. *Inorg. Chem.* **2017**, *56*, 1546−1557.
(42) *SADABS VX*; Bruker AXS Inc.: Madison, WI, 2004.
(43) *SAINT VX*; Bruker AXS Inc.: Madison, WI, 2004.
(44) *SHELXTL VX*; Bruker AXS Inc.: Madison, WI, 2013.
(45) Sheldrick, G. M. A short history of SHELX. *Acta Crystallogr., Sect. A: Found. Crystallogr.* **2008**, *64*, 112−122.
(46) Spek, A. L. Structure validation in chemical crystallography. *Acta Crystallogr., Sect. D: Biol. Crystallogr.* **2009**, *65*, 148−155.
(47) O'Connor, C. J. Magnetochemistry—Advances in Theory and Experimentation. *Prog. Inorg. Chem.* **1982**, *29*, 203−283.
(48) Evans, D. F. The determination of the paramagnetic susceptibility of substances in solution by nuclear magnetic resonance. *J. Chem. Soc.* **1959**, 2003−2005.
(49) Stancanello, J.; Terreno, E.; Castelli, D. D.; Cabella, C.; Uggeri, F.; Aime, S. Development and validation of a smoothing-splines-based correction method for improving the analysis of CEST-MR images. *Contrast Media Mol. Imaging* **2008**, *3*, 136−149.
(50) Dixon, W. T.; Ren, J.; Lubag, A. J. M.; Ratnakar, J.; Vinogradov, E.; Hancu, I.; Lenkinski, R. E.; Sherry, A. D. A concentration-independent method to measure exchange rates in PARACEST agents. *Magn. Reson. Med.* **2010**, *63*, 625−632.
(51) Di Vaira, M.; Mani, F.; Stoppioni, P. Eight-co-ordination in manganese(II) and iron(II) complexes with a pyrazole-functionalised tetraazamacrocycle. *J. Chem. Soc., Dalton Trans.* **1992**, 1127−1130.
(52) Koch, W. O.; Barbieri, A.; Grodzicki, M.; Schünemann, V.; Trautwein, A. X.; Krüger, H.-J. Eight-Coordinate Iron(II) and Iron(III) Ions in Complexes with Distorted Dodecahedral FeN8 Environments: Synthesis and Structures of Bis(2,11-diaza[3.3](2,6)-pyridinophane)iron Complexes. *Angew. Chem., Int. Ed. Engl.* **1996**, *35*, 422−424.
(53) Adam, R.; Ballesteros-Garrido, R.; Ferrer, S.; Abarca, B.; Ballesteros, R.; Real, J. A.; Munoz, M. C. From six-coordinate to eight-coordinate iron(ii) complexes with pyridyltriazolo-pyridine frameworks. *CrystEngComm* **2016**, *18*, 7950−7954.
(54) Vojtíšek, P.; Cígler, P.; Kotek, J.; Rudovský, J.; Hermann, P.; Lukeš, I. Crystal Structures of Lanthanide(III) Complexes with Cyclen Derivative Bearing Three Acetate and One Methylphosphonate Pendants. *Inorg. Chem.* **2005**, *44*, 5591−5599.
(55) Platas-Iglesias, C. The Solution Structure and Dynamics of MRI Probes Based on Lanthanide(III) DOTA as Investigated by DFT and NMR Spectroscopy. *Eur. J. Inorg. Chem.* **2012**, *2012*, 2023−2033.
(56) Meier, K.; Rihs, G. Reactions in the Ligand Sphere of Iron(II): Synthesis of Crown Ethers. *Angew. Chem., Int. Ed. Engl.* **1985**, *24*, 858−859.
(57) Beer, P. D.; Drew, M. G. B.; Leeson, P. B.; Ogden, M. I. Versatile cation complexation by a calix[4]arene tetraamide (L). Synthesis and crystal structure of [ML][ClO4]2[middle dot]nMeCN (M = FeII, NiII, CuII, ZnII or PbII). *J. Chem. Soc., Dalton Trans.* **1995**, 1273−1283.
(58) Bill, E. *JulX version 1.4.1; Magnetic Susceptibility Simulation Software*; Max-Plank Institute: Germany, 2008.
(59) Weber, B.; Walker, F. A. Solution NMR Studies of Iron(II) Spin-Crossover Complexes. *Inorg. Chem.* **2007**, *46*, 6794−6803.
(60) Carabineiro, S. A.; Bellabarba, R. M.; Gomes, P. T.; Pascu, S. I.; Veiros, L. F.; Freire, C.; Pereira, L. C. J.; Henriques, R. T.; Oliveira, M. C.; Warren, J. E. Synthesis, Structure and Magnetic Behavior of Five-Coordinate Bis(iminopyrrolyl) Complexes of Cobalt(II) containing PMe3 and THF Ligands. *Inorg. Chem.* **2008**, *47*, 8896−8911.
(61) Forshaw, A. P.; Smith, J. M.; Ozarowski, A.; Krzystek, J.; Smirnov, D.; Zvyagin, S. A.; Harris, T. D.; Karunadasa, H. I.; Zadrozny, J. M.; Schnegg, A.; Holldack, K.; Jackson, T. A.; Alamiri, A.; Barnes, D. M.; Telser, J. Low-Spin Hexacoordinate Mn(III): Synthesis and Spectroscopic Investigation of Homoleptic Tris(pyrazolyl)borate and Tris(carbene)borate Complexes. *Inorg. Chem.* **2013**, *52*, 144−159.
(62) Aime, S.; Barge, A.; Delli Castelli, D.; Fedeli, F.; Mortillaro, A.; Nielsen, F. U.; Terreno, E. Paramagnetic Lanthanide(III) complexes as pH-sensitive chemical exchange saturation transfer (CEST) contrast agents for MRI applications. *Magn. Reson. Med.* **2002**, *47*, 639−648.
(63) Olatunde, A. O.; Cox, J. M.; Daddario, M. D.; Spernyak, J. A.; Benedict, J. B.; Morrow, J. R. Seven-coordinate Co(II), Fe(II) and six-coordinate Ni(II) amide-appended macrocyclic complexes as ParaCEST agents in biological media. *Inorg. Chem.* **2014**, *53*, 8311−8321.
(64) Ratnakar, S. J.; Woods, M.; Lubag, A. J. M.; Kovács, Z.; Sherry, A. D. Modulation of Water Exchange in Europium(III) DOTA−Tetraamide Complexes via Electronic Substituent Effects. *J. Am. Chem. Soc.* **2008**, *130*, 6−7.
(65) Opina, A. C. L.; Wu, Y.; Zhao, P.; Kiefer, G.; Sherry, A. D. The pH sensitivity of − NH exchange in LnDOTA−tetraamide complexes varies with amide substituent. *Contrast Media Mol. Imaging* **2011**, *6*, 459−464.
(66) van Zijl, P. C. M.; Yadav, N. N. Chemical exchange saturation transfer (CEST): What is in a name and what isn't? *Magn. Reson. Med.* **2011**, *65*, 927−948.
(67) Delli Castelli, D.; Ferrauto, G.; Di Gregorio, E.; Terreno, E.; Aime, S. Sensitive MRI detection of internalized T1 contrast agents using magnetization transfer contrast. *NMR Biomed.* **2015**, *28*, 1663−1670.
(68) Nicholls, F. J.; Ling, W.; Ferrauto, G.; Aime, S.; Modo, M. Simultaneous MR imaging for tissue engineering in a rat model of stroke. *Sci. Rep.* **2015**, *5*, 14597.

DOI: 10.1021/acs.inorgchem.7b01629
Inorg. Chem. 2017, 56, 12206−12213